Tensile and Compressive Response of Tungsten g-TPMS Lattice Structures

Zahabul Islam^{1,*}, Tanvir Ahmed¹, Mohammad Mayyas², Mohammed Abouheaf²

¹Mechanical and Manufacturing Engineering Program, School of Engineering, Bowling Green State University, Bowling Green, OH, 43403, USA

²Robotics Engineering, School of Engineering, Bowling Green State University, Bowling Green, OH, 43403, USA

Abstract

The present study explores the mechanical behavior of tungsten (W) gyroid Triply Periodic Minimal Surface (g-TPMS) lattice structures through atomistic simulations, focusing on models with varying lattice thickness or simply volume fractions. It examines the mechanical behavior of these structures under both tensile and compressive loads. The research demonstrates that strength and ductility in g-TPMS can be adjusted through design, showcasing unique behaviors not found in bulk materials. A relationship between elastic modulus and volume fraction is established, providing coefficients for multi-scale modeling and simulation. W g-TPMS structures with higher volume fractions exhibit increased tensile strength, peaking at approximately 7.6 GPa for structures with a 59% volume fraction. The study further reveals that temperature variations significantly affect the mechanical response, with tensile strength decreasing from 4.5 GPa at 300K to below 2.0 GPa at 3000K. Additionally, helium embrittlement is shown to markedly reduce tensile strength, with a 15% helium interstitial concentration leading to a 60% reduction in peak stress. These findings emphasize the potential of tailored W g-TPMS materials for advanced applications like nuclear fusion reactors.

Keywords: Tungsten (W), gyroid Triply Periodic Minimal Surface (g-TPMS), volume fractions, strength, helium embrittlement

1.0 Introduction

Tungsten stands out in the periodic table due to its extraordinary physical and chemical properties. It has the highest melting point of all metals (3,422 °C or 6,192 °F), exceptional hightemperature strength, and remarkable thermal conductivity [1]. These characteristics make tungsten an element of significant interest in various high-tech applications, especially in extreme environments [1-5]. In the quest for sustainable and clean energy, nuclear fusion presents a promising frontier, offering the potential for abundant energy with minimal environmental impact. Tungsten, with its highest melting point among metals and exceptional thermal conductivity, stands as a frontrunner for plasma-facing materials in fusion reactors [1]. However, a significant challenge emerges in the form of helium (He) irradiation and embrittlement effects [6-10]. When exposed to the intense neutron flux characteristic of fusion reactions, tungsten undergoes transmutation reactions, leading to the generation of helium within its crystalline structure. This process initiates a series of microstructural changes, critically impacting the performance and longevity of the material. Helium accumulation in tungsten can lead to embrittlement, swelling, and surface blistering, posing a severe risk to the integrity and functionality of reactor components [11-17]. Understanding and mitigating these effects is crucial for the advancement and viability of fusion technology.

The intricate world of lattice structures represents a confluence of geometry, materials science, and engineering, offering unparalleled opportunities in the design and application of advanced materials. Lattice structures, characterized by their repetitive network of nodes and struts or plates, present a unique combination of lightweight characteristics and mechanical strength, making them highly desirable in various applications, from aerospace engineering to biomedical implants [18-20]. The advent of advanced manufacturing techniques, especially additive manufacturing (also known as 3D printing), has further unlocked the potential of complex lattice designs. Up to now, there have been significant advancements in fabrication of lattice structures [21-35]. Recent studies have shown promising results using additive manufacturing techniques, such as 3D printing, to create TPMS structures at micro-nano scale. Among the various types of lattice structures, gyroid Triply Periodic Minimal Surface (g-TPMS) lattices have emerged as a particularly prominent category. These structures are defined by their continuous surface with a periodic minimal surface area, resulting in a highly efficient use of material while maintaining structural integrity. TPMS lattices, such as those based on Gyroid, Diamond, and Schwarz

Primitive geometries, offer several distinct advantages over other lattice structures. However, the prominence of TPMS lattice structures lies in their ability to address complex engineering challenges while optimizing material properties. From a mathematical perspective, TPMS structures are notable for their surfaces with zero mean curvature and local area-minimizing properties. Within the TPMS family, the gyroid structure is the most extensively studied and has been naturally observed in the wing scales of various butterflies. Recent research has provided extensive insights into the physics underlying the mechanical, thermal, optical, and electromagnetic properties of gyroid cellular materials [24, 36-39]. Their versatility and efficiency make them a subject of intense research and innovation, particularly in fields where material performance is critical under extreme conditions, such as in aerospace and nuclear fusion applications [40-44]. Thus, as we continue to push the boundaries of advanced manufacturing, g-TPMS lattice structures stand at the forefront, offering novel solutions to some of the most demanding technical challenges. The fabrication of g-TPMS at the nanoscale is indeed an ongoing challenge, primarily due to the complex topologies of these structures. However, recent advancements in nanoscale fabrication techniques offer promising pathways toward realizing TPMS structures at this scale. Additionally, the advancements in additive manufacturing, particularly photopolymerization-based two-photon lithography (TPL), have shown the capability to print complex 3D structures with sub-micrometer resolution [45]. This technique holds significant promise for the fabrication of nanoscale g-TPMS structures. The findings can be considered as promising and indicate that with ongoing advancements in nanoscale fabrication techniques. At present, though there is not only a lack of mature manufacturing technologies capable of directly manipulating individual atoms to create materials, but also an absence of computational approaches that can design materials atom-by-atom. Thus, achieving atomic-level precision in material design will unlock the full potential of matter, opening immense opportunities across various scientific and engineering fields. The significance of the proposed simulations method lies in its ability to provide a platform for computers to design novel materials atom-byatom. In addition, nanoscale study can be furthered used to create a wide range of novel nanomaterials and nanomachines with unprecedented performance.

The innovative application of tungsten (W) with Triply Periodic Minimal Surface (g-TPMS) lattice structures can be used as a promising avenue for addressing helium (He) irradiation challenges in nuclear reactors. The unique geometry of g-TPMS structures could potentially

mitigate the detrimental effects of helium accumulation in tungsten, a critical concern in fusion reactor environments. In a fusion reactor, tungsten components are subjected to intense neutron bombardment, leading to the transmutation of tungsten atoms. This process results in helium bubble formation within the tungsten matrix, causing embrittlement, swelling, and surface blistering, which compromise the integrity and functionality of the materials [44, 46, 47]. The g-TPMS lattice structure, with its intricate and repetitive geometric patterns, can offer a novel solution to this problem. This innovative approach exemplifies the intersection of advanced manufacturing and nuclear engineering, offering a path toward more durable and reliable structures for the future of nuclear fusion technology.

Molecular dynamics (MD) simulation represents a transformative approach in the study of metals, offering insights into their mechanical properties, irradiation damage, corrosion resistance, and processing effects to name a few [48-52]. This technique allows the simulation of metal, alloys, polymers, and composites [53-58] enabling researchers to delve into the atomic-scale phenomena that govern the macroscopic properties of materials. Thus, MD simulations can serve as a powerful tool, offering detailed and accurate predictions of the mechanical response. This approach not only enhances our fundamental understanding of material properties at the atomic level [59-62] but also drives innovation in material design and application across various industries.

In the following sections, the present study employs MD simulation to investigate: (1) mechanical response of W g-TPMS lattice structure under tensile and compressive loading, (2) development of a relationship between volume fraction and mechanical properties, (3) examining the impact of temperature on mechanical properties, and (4) assessing the effect of helium interstitials on W g-TPMS and bulk tungsten.

2.0 Materials and Methods

The present study uses the Embedded Atom Method (EAM) potential [63] to study the W g-TPMS lattice structure using LAMMPS code [64]. The EAM potential is mathematically defined by the following expressions:

$$U = \sum_{i} F(\rho_{i}) + \frac{1}{2} \sum_{i} \sum_{i \neq j} \varphi_{ij}$$
 (1)

where, U represents the total energy of the system, $F(\rho_i)$ is the embedded energy as a function of the electron density, ρ_i denotes the electron density contributed by the host atoms, and ϕ_{ij} is the pairwise interaction potential dependent on the distance between atoms i and j.

A gyroid triply periodic minimal surfaces (g-TPMS) lattice structures with variable wall thickness, t (Fig. 1a-1d) has been considered for this present study. The g-TPMS equations delineate 3D surfaces that can be regarded as the demarcation between the empty space (Porous/hollow) and the solid material. By identifying the U=0, iso-surface of these equations, it is possible to generate matrix phase gyroid structures with numerous cells counts and volume proportions:

$$U = \left[\cos(k_x x)\sin(k_y y) + \cos(k_y y)\sin(k_z z) + \cos(k_z z)\sin(k_x x)\right]^2 - t^2$$
 (2)

$$k_i = 2\pi \frac{n_i}{L_i} \text{ (where, } i = x, y, z) \tag{3}$$

Where, n_i represents the quantities of cell repetitions along the x, y, and z axes, while L_i denotes the size of the structure in those respective directions. The density of the g-TPMS structure can be written as a function of thickness and periodicity using eq. (4):

$$\rho^* = f(t, k_i) \tag{4}$$

In this present study, four g-TPMS models were modeled using nTop software [65] as shown in Fig. 1a-1d, and using this model, four W g-TPMS structures with shell thicknesses of 1 nm, 2 nm, 2.5 nm, and 3 nm were created. The gray color in Fig. 1a-1d indicates a solid body and empty space (white color) indicates a void. Hence, the volume fraction (ρ^*) can be defined as the volume of the gray solid to the total volume of the cell. The corresponding volume fractions at shell thicknesses of 1 nm, 2 nm, 2.5 nm, and 3 nm are found to be 19.3%, 38.9%, 48.9%, and 59% respectively. The corresponding atomistic models of W g-TPMS are depicted in Fig. 1e-1h. In the present study, a time step of 1 fs and a simulation pressure of 1 bar was maintained during all simulations. The dimensions of the body-centered cubic (bcc) Tungsten simulation cell were approximately set to 200 Å x 200 Å x 200 Å with a total number of atoms were 549,250. The lattice constant of the BCC unit cell of W was set as at 3.165Å. As illustrated in Fig. 2b, the stress-strain responses are consistent across different atom numbers, demonstrating that the results are stable due to the use of periodic boundary conditions. This approach ensures that the mechanical properties are not significantly affected by the number of atoms, allowing optimization of the

simulation time without compromising the accuracy of the results. For present simulations, 549250 atoms as an optimal balance, providing reliable results while maintaining computational efficiency. This choice also allows for conducting comprehensive studies within a practical timeframe, ensuring that the simulations are both effective and resource efficient. At the beginning

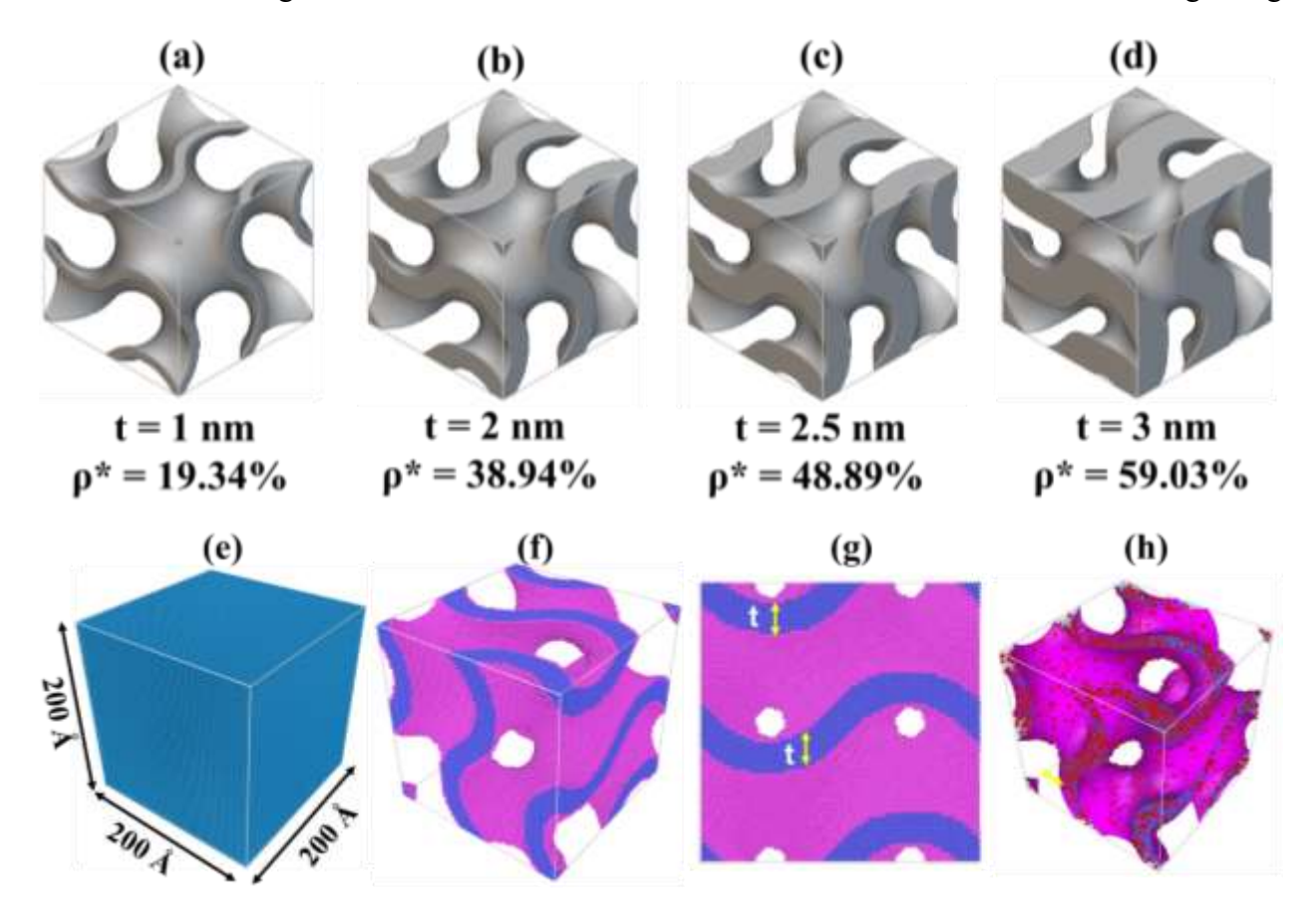


Figure. 1. (a)-(d) Computer model of g-TPMS lattice structure with different volume fraction alternatively volume fraction, Atomistic model with a cell dimension of 200Å×200Å×200Å: (e) Bulk W, (f) W g-TPMS, (g) W g-TPMS side view showing lattice thickness (t), and (h) He interstitials in W g-TPMS lattice (pin color surface has been introduced to show g-TPMS surface. of the simulation, all structures were brought to an energy-optimized state using conjugate-gradient (CG) method. Periodic boundary conditions were applied in all directions. Subsequently, NPT dynamics were carried out for several thousands of steps to relax the energy-minimized atomistic model. All the simulations were carried out with the aid of the LAMMPS simulation package [17]. Prior to the simulation, the strain rate effect on the mechanical properties was studied as described in section 3.1. A strain rate of 10^{-9} s⁻¹ was chosen based on the outcome of the strain rate effect

on mechanical properties. During the tensile and compressive simulation, NPT dynamics were deployed for the time integration. The present study also considers varying temperatures effects, specifically at 1000 K, 2000 K, and 3000 K, on the mechanical response of the g-TPMS structure. Furthermore, the effect of Helium interstitial on the mechanical response of W g-TPMS lattice structures were investigated with 1%, 5%, 10%, and 15% Helium interstitial.

3.0 Results and Discussion

3.1. Effect of Strain Rate and Simulation Cell Size

3.1.1 Effect of Strain Rate on the Tensile Response

The stress-strain plot for the g-TPMS lattice structure with volume fraction 38.9% subjected to tensile loading at different strain rates namely 10⁸s⁻¹, 5×10⁸s⁻¹, 10⁹s⁻¹, 5×10⁹s⁻¹, 10¹⁰s⁻¹, and 5×10¹⁰s⁻¹, as shown in Fig. 2a. The stress-strain curves illustrate several distinct features as follows: As the strain rate increases above $5 \times 10^9 \text{s}^{-1}$, there is a corresponding increase in the peak tensile stress and tensile stress variation with strain inconsistency. The curve corresponding to 10^{10} s⁻¹, and 5×10^{10} s⁻¹ reaches the highest peak stress, while the curve below 5×10⁹s⁻¹, shows consistent peak stress, failure strain as well as elastic modulus. The increased tensile strength at higher strain rates could be explained by the strain rate-dependent mechanisms of the material, such as viscoelasticity or strain rate-sensitive dislocation dynamics. At higher strain rates, there is less time for atoms to relax or dislocations to move and for voids or cracks to nucleate and grow, resulting in higher apparent strength. For dynamic applications where TPMS structures are subjected to high strain rates, such as impact loading [66], the structures will behave differently than under quasi-static conditions. However, the material at lower strain rates shows less fluctuation in stress and the stress-strain response is consistent. The initial slope of the stressstrain curve, which is indicative of the elastic modulus, below 5×10⁹s⁻¹ strain rate shows a clear and consistent trend with respect to the strain rate. This suggests that the elastic properties below the $5\times10^9 \mathrm{s}^{-1}$ strain rate may not be sensitive to the strain rate. It is noteworthy that the length scale and timescale used in classical molecular dynamics simulations differ significantly from those used in experiments [66]. Moreover, unlike the g-TPMS samples investigated in this study, realworld bulk samples contain defects such as vacancies, dislocations, grain boundaries, and multiple phases. These factors may also influence the deformation behaviors observed in experimental conditions [66].

3.1.2 Effect of Simulation Cell Size on the Tensile Response

To investigate the effect of simulation cell size on the tensile stress-strain curves for the g-TPMS lattice structure obtained from atomistic simulations with varying numbers of atoms namely 54000, 250000, 549250, and 843750 (or supercells with repetition of 35, 50, 65, and 75 unit cell respectively) reveal the effect of simulation cell size on mechanical response. All curves as shown in Fig. 2b exhibit a similar trend and difficult to be distinguished from each other, suggesting that the elastic modulus is not influenced by the certain number of atoms used in the simulation. This consistency indicates that the intrinsic material properties are well-represented across different simulation cell sizes, primarily due to the periodic boundary conditions imposed during the simulation that mitigate size-dependent effects. Furthermore, the ultimate tensile strength (UTS) is observed to be approximately 26.3 GPa for four simulations, highlighting that the critical stress at which the material begins to yield remains stable regardless of the simulation cell size. Consequently, these findings suggest that atomistic simulations of g-TPMS lattice structures can achieve accurate representations of their elastic properties and yield strength with a range of atom counts, allowing for flexibility in balancing computational efficiency and simulation detail.

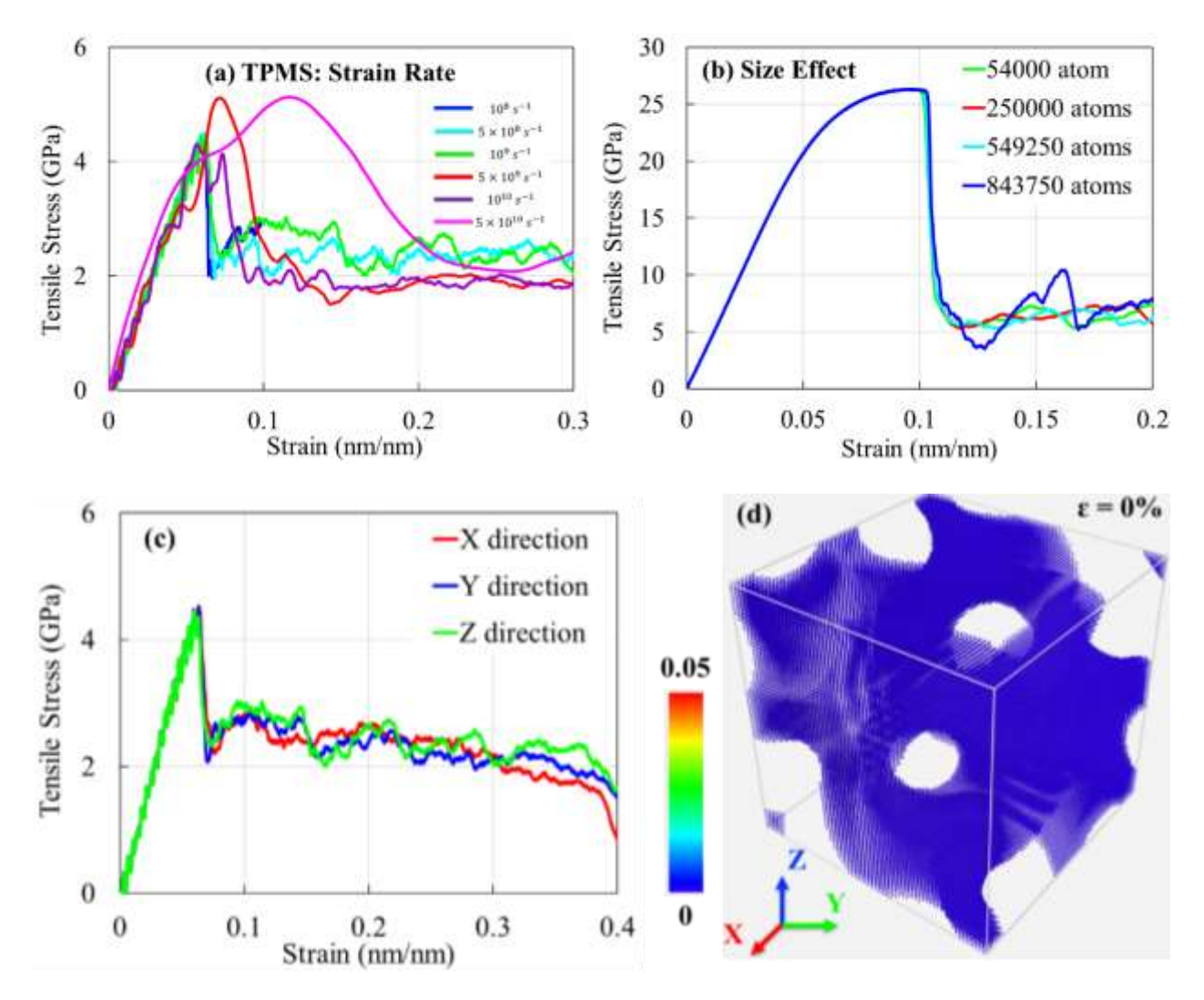
Moreover, it is recognized that experimental validation is important; however, it is worth noting that atomistic simulations offer valuable insights that are often challenging to obtain experimentally, particularly at the nanoscale. To validate the simulation results, additional MD simulations were conducted on tungsten (W) samples. Based on the elastic calculation, bulk modulus, shear modulus and Poisson's ratio of W are found to be 307 GPa, 160 GPa and 0.2796, which are in well agreement with the existing literatures [67, 68]. Thus, the results obtained from the elastic constant calculations demonstrate the accuracy of the simulations.

3.2 Mechanical properties

3.2.1 Tensile Behavior

Gyroid TPMS (g-TPMS) structures are considered for this study have a uniform distribution of curvature and symmetry in all directions as shown in Fig. 2c. To investigate the direction dependent tensile and compressive response of the g-TPMS W structure, one model of gyroid g-TPMS with 38.9% volume fraction (i.e., t = 2 nm) was chosen and further investigated. The loading direction in X, Y and Z direction are shown in Fig. 2d. The tensile response of the W g-TPMS lattice structure in the X, Y, and Z directions are identical, as evidenced by the

overlapping stress-strain curves obtained in all three directions (Fig. 2c). It is obvious that the initial elastic region is linear in all three directions, suggesting that the material behaves uniformly under tensile stress until the yield point. The stress peaks at around 4.45 GPa for each direction, indicating that ultimate strength of the g-TPMS is independent of the loading direction. The calculated Elastic modulus is found to be 78.5 GPa at 38.9% volume fraction. To investigate the deformation mechanism, shear strain distribution in the model is depicted in Fig. 2d-2g. The shear strain is high and localized at the locations of the g-TPMS lattice indicated by the red arrow in Fig. 2e-2g. The yielding will take place around these shear band areas and has been corroborated by the shear strain distribution in Fig. 2f and 2g. The shear strain band appears at 45° angle with the tensile loading direction as shown in Fig. 2g. Post-yielding further induce necking at these locations, where shear strain is found to be maximum.



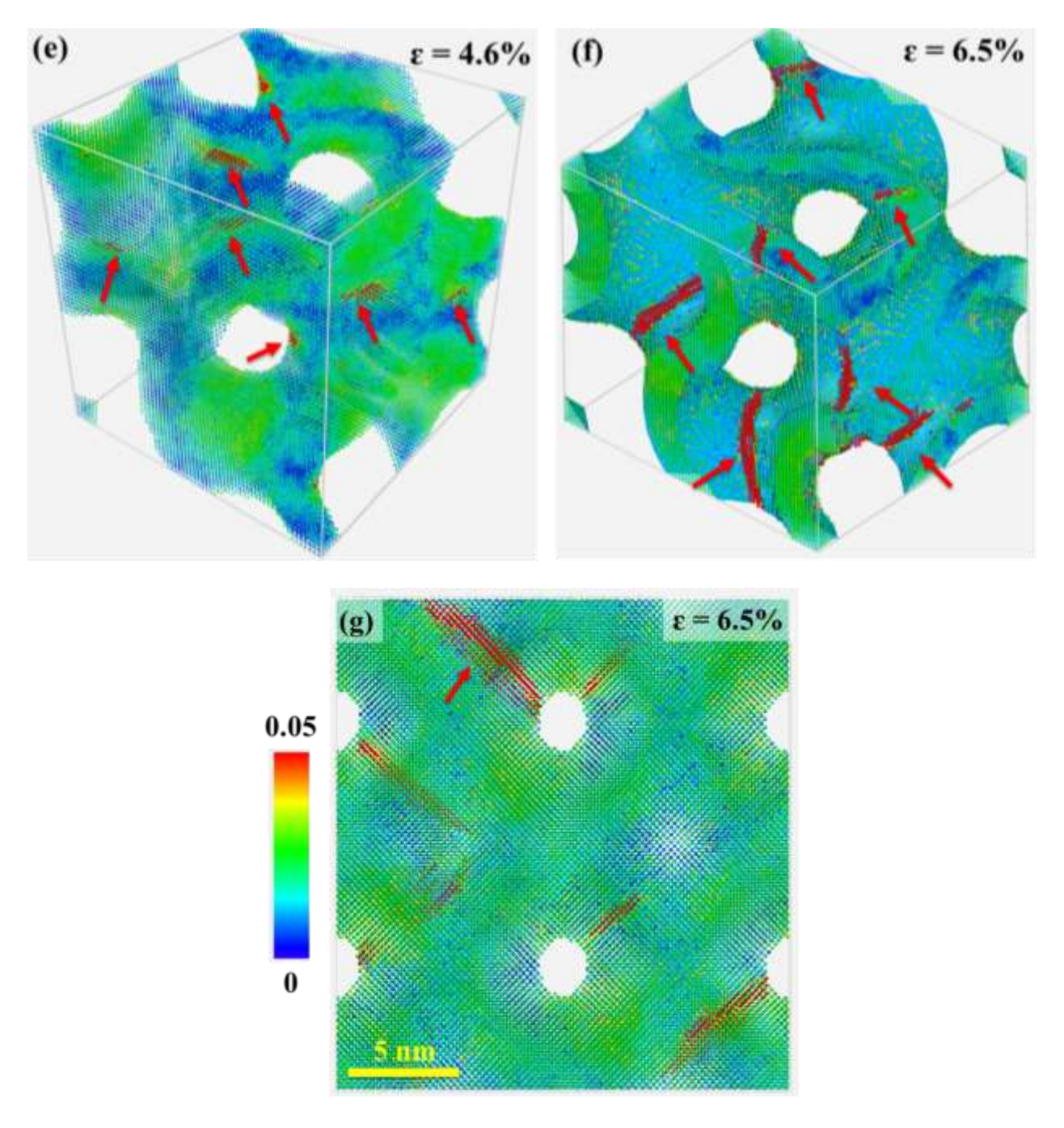
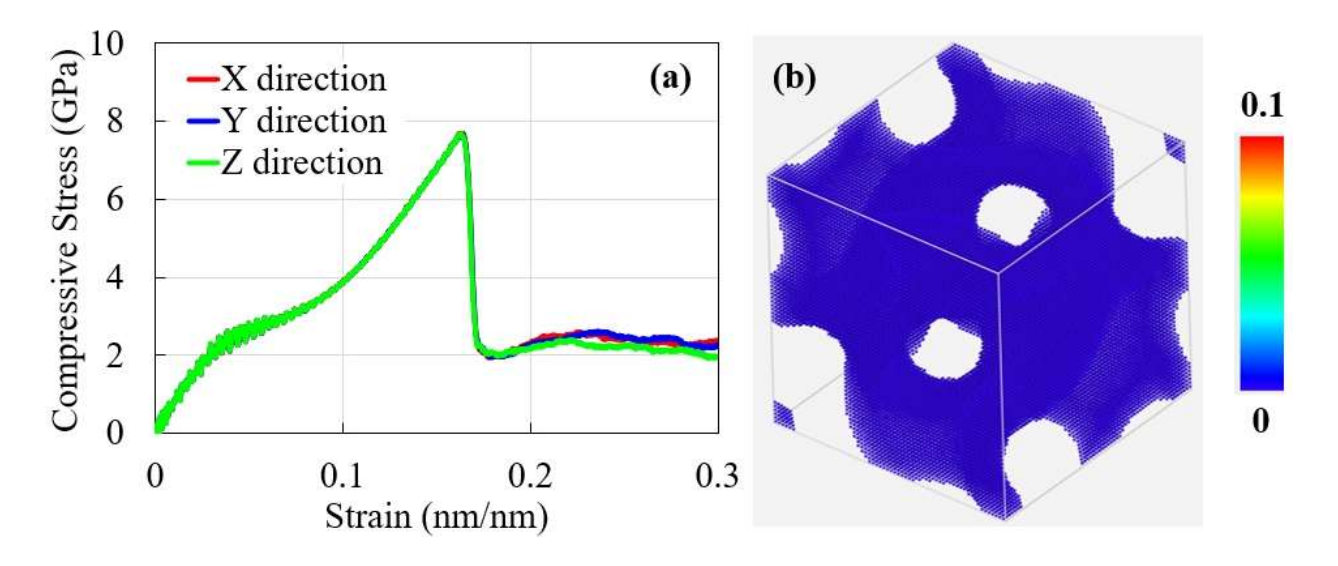


Figure. 2. Tensile response of W g-TPMS lattice: (a) Strain rate effect on mechanical properties, (b) Simulation cell size effect on mechanical properties, (c) Tensile response of W g-TPMS lattice with shell thickness 2nm (volume fraction 38.9%), Shear stress distribution on the lattice at: (d) strain = , (e) strain = 0, (e) strain = 0, and (f) onset of plastic deformation at strain = 0, and (g) shear band at 0.

The similarity in the stress-strain curves for all three directions (i.e., X, Y, and Z) implies that the W g-TPMS lattice structure is equally strong and ductile along these three directions. Unlike most of the lattice structures, this unique mechanical property is beneficial for engineering applications. The peak stress values being consistent across all three loading directions indicates that the g-TPMS structure will have uniform and predictable performance under tensile loading, which is essential for designing reliable and robust components. For structural applications, especially in next-generation fusion reactors, materials are often required to have predictable properties in all directions. Thus, this unique mechanical behavior of the tungsten g-TPMS lattice structure makes it a strong candidate for such applications.

3.2.2 Compressive Behavior

While the similar mechanical behavior in X, Y and Z directions is evident from the tensile loading, further studies have been conducted to investigate the response of g-TPMS under compressive loading. The compressive loading of the W g-TPMS lattice structure in the X, Y, and Z directions yielded stress-strain curves that show remarkably consistent across all three directions. The identical mechanical response of the material is evident from the overlapping curves as shown in Fig. 3a. All three directions show almost identical peak stress around 7.68 GPa. After yielding, all three curves demonstrate a sharp reduction in stress at a strain of 16.4%, indicating a similar post-yielding behavior across all directions. After post-yielding, the material shows a plateau at around 2 GPa for all directions.



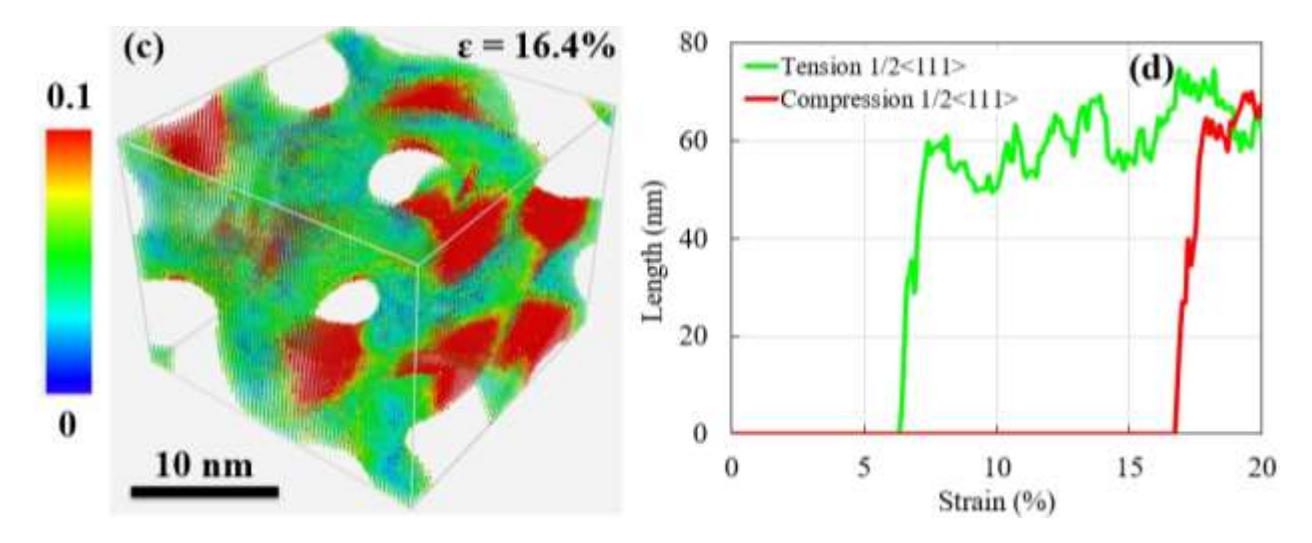


Figure. 3. (a) Compressive response of W g-TPMS lattice with shell thickness 2nm (volume fraction 38.9%), Shear stress distribution on the lattice at (b) strain = 0, (c) onset of plastic deformation at strain = 16.4%, and (d) $\frac{1}{2} < 111 >$ dislocation progression during the deformation.

To investigate the deformation mechanism in g-TPMS, dislocation analysis was conducted and shown in Fig. 3d. For both tensile and compressive loading, post-yielding suggests that plastic deformation is governed by ½ <111> dislocations. In the case of compression testing, ½ <111> dislocations initiate at 16.4% in the g-TPMS structure, whereas the onset of plastic deformation initiates around 6.4% followed by the formation of ½ <111> dislocation during the tensile testing. High plastic strain observed during the compression loading suggests that the g-TPMS structure can deform plastically and potentially absorb more energy in compression than tensile loading condition. The following section investigates the effect of volume fraction on the mechanical properties of the W g-TPMS lattice. Further examination of the volume fraction will provide an in-depth understanding of the structure-property relationship.

3.3 Effect of volume fraction on Mechanical response

In this section, the effect of the lattice thickness or volume fraction on the mechanical response of the g-TPMS has been investigated. For this study, four lattice structures with different volume fractions were considered as mentioned in section 2. The W g-TPMS lattice structures with wall thicknesses of 1 nm, 2 nm, 2.5 nm, and 3 nm correspond to 19.3%, 38.9%, 48.9%, and 59% volume fractions respectively as shown in Fig. 4a. The present study, indicates that the W g-TPMS structure with 3 nm shell thickness (59% volume fraction) exhibits the highest tensile strength, peaking at approximately 7.6 GPa. This indicates a substantial material strength at a high-

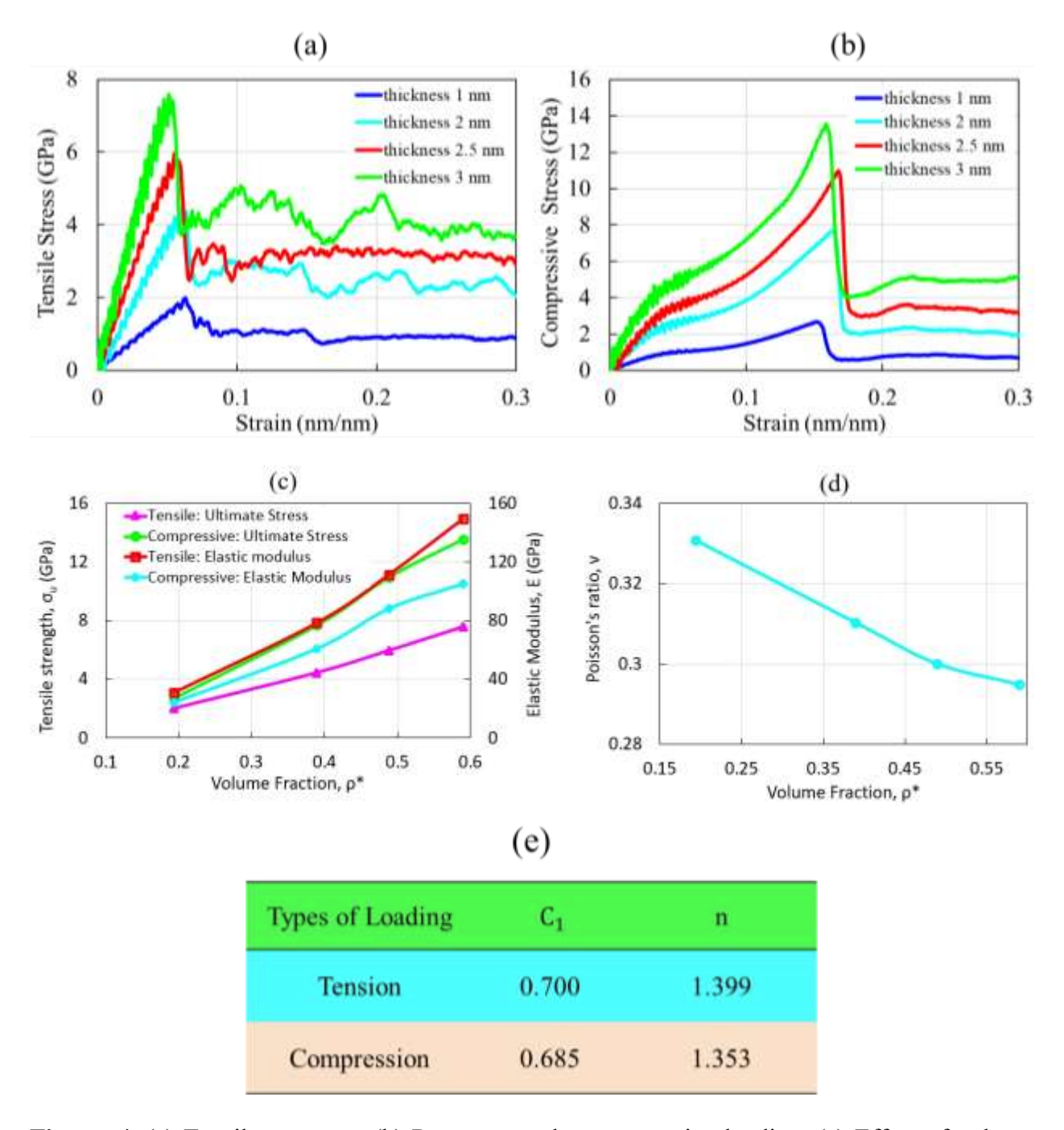


Figure. 4. (a) Tensile response, (b) Response under compressive loading, (c) Effect of volume fraction Elastic modulus and ultimate strength, and (d) Factors for eq. (2) (calculated for Elastic modulus).

volume fraction showing significant resistance to deformation under tensile loading. The 2.5 nm (48.9% volume fraction) sample reached ultimate stress slightly lower than that of the 3 nm sample. Moreover, the 2 nm structure (38.9% volume fraction) showed a further reduction in

ultimate tensile strength (UTS). The 1 nm structure (19.3% volume fraction), while possessing the lowest UTS at around 2 GPa, demonstrated a little more ductility compared to the other three structures. The results suggest an inverse relationship between wall thickness i.e., volume fraction and ductility in g-TPMS structure. The 1 nm structure, despite its lower strength, shows a greater ability to deform. Across the sample thickness, the modulus decreases with the decrement in thickness, suggesting that the stiffness of the g-TPMS is a function of g-TPMS shell thickness or volume fraction. Unlike grain size-dependent strengthening often seen in nanomaterials [69-71], g-TPMS is modeled using a single crystal (no defects like vacancy, dislocations, grain boundaries etc.,). Thus, instead of grain size-dependent strengthening, volume fraction-dependent strengthening is observed.

In addition to the tensile and compressive response, Poisson's ratio of the g-TPMS W structures was calculated using a custom MATLAB code. The calculated graphs are shown in the supplementary section S1. The calculated Poisson's ratio as a function of volume fraction is depicted in Fig. 4d. The plot demonstrates a clear trend where the Poisson's ratio of the g-TPMS lattice decreases as the volume fraction increases. The highest Poisson's ratio is observed at the lowest volume fraction (approximately 19.3%), with a value near 0.34. As the volume fraction increases to approximately 59%, the Poisson's ratio decreases to a value near 0.294, which is close to 0.29 i.e., bulk W Poisson's ratio [67, 68]. The Poisson's ratio is a measure of the ability of g-TPMS lattice to undergo lateral expansion or contraction in response to longitudinal strain. The decreasing trend of Poisson's ratio with an increasing volume fraction may be explained by the densification of the lattice structure. As the volume fraction increases, the TPMS lattice becomes denser, which generally leads to a stiffer and less compliant structure. This densification reduces the ability of the material to deform laterally, resulting in a lower Poisson's ratio. The decrement of the slope in Fig. 4a corroborates this hypothesis. This behavior is relevant for the design and application of g-TPMS structures in engineering. This trend could be further utilized in the targeted design of materials with specific mechanical properties. By adjusting the volume fraction, one can tailor the Poisson's ratio to meet the requirements of a particular application. It is noteworthy that the relationship between volume fraction and Poisson's ratio could be affected by the specific geometry of the TPMS lattice, and different TPMS geometries may exhibit different trends. Future studies could expand on these results by exploring different TPMS geometries to develop a more comprehensive understanding of the relationship between volume fraction and Poisson's ratio...

The nano-architected materials demonstrate that through careful design, both strength and ductility can be tuned in the same material. These findings indicate that at the nanoscale, g-TPMS structures can exhibit unique tensile behaviors not seen in bulk materials, underscoring the impact of nano-structuring on material properties. W g-TPMS lattice structures demonstrate a clear trend where increased wall thickness or volume fraction leads to increased tensile strength but reduced ductility. Conversely, thinner walls offer higher ductility but at the expense of peak tensile strength. Thus, mechanical properties such as elastic modulus or Young's modulus, and tensile strength can be expressed as a function of volume fraction as follows [72, 73]:

$$\mathbf{E}^* = \mathbf{C}_1(\mathbf{\rho}^*)^n \tag{5}$$

$$E^* = \frac{E_{g-TPMS}}{E_{Bulk}} \tag{6}$$

$$\rho^* = \frac{V_{g-TPMS}}{V_{Bulk}} \tag{7}$$

The calculated co-efficient C_1 and n for g-TPMS have been shown in Fig. 4d for both tensile and compressive loading cases. These parameters can provide further guidelines for finite element or multi-scale simulations.

The stress-strain curves obtained from the compressive loading of W g-TPMS lattice structures exhibit clear distinctions in mechanical response as a function of wall thickness or volume fraction. The 3 nm structure (59% volume fraction) shows the highest ultimate stress at approximately 13.5 GPa, demonstrating considerable strength before the failure. Both 2.5 nm and 2 nm structures reached a peak stress lower than the 3 nm structure. The ultimate stress of the 1 nm structure was markedly lower than the other three structures. Across all thicknesses, the initial linear response is a characteristic of elastic deformation, where the elastic modulus of the g-TPMS, is observable. The different slopes in this phase across the different thicknesses suggest the elastic modulus of the g-TPMS geometry is a function of volume fraction. This relation can be expressed by eqn. 5 using the data depicted in Fig. 4d. The ultimate compressive strength decreases with the thinning of the g-TPMS walls or volume fraction. As mention in the previous section, unlike grain size-dependent strengthening [69-71], volume fraction-dependent strengthening is observed in present study due to the defects free structures like vacancy, dislocations, grain boundaries etc.,). In addition to this effort in developing a relationship between elastic modulus and volume fraction

for the W g-TPMS lattice structure, an attempt has been made to correlate tensile and compressive strength with the volume fraction as expressed by eqns. (8) and (9).

The ultimate tensile strength of the g-TPMS structure in terms of volume fraction can be written as:

$$\sigma_{\text{TU}}^{\ *} = 0.531(\rho^{*})^{1.189} \tag{8}$$

The ultimate compressive strength of the g-TPMS structure in terms of volume fraction can be expressed as:

$$\sigma_{\text{CU}}^* = 0.254(\rho^*)^{1.471} \tag{9}$$

These results imply that selecting an appropriate g-TPMS wall thickness or volume fraction can help to tailor the mechanical performance to specific application requirements. The high strength of thicker g-TPMS structures may be desirable for structural components, while the increased ductility of thinner structures could be beneficial for applications requiring enhanced surface area, such as heat transfer applications.

In the following section, the mechanical response of W g-TPMs structure under thermal load and Helium irradiation will be investigated. For the following studies, the W g-TPMS structure with a 38.9% volume fraction will be only considered as a representative model.

3.4 Mechanical response under thermal load

The mechanical response of W g-TPMS lattice structure with a volume fraction of 38.9% under tensile loading was evaluated at four different temperatures: 300K, 1000K, 2000K, and 3000K (~ 0.8T_m). The tensile response as shown in Fig. 5a indicates dependence of mechanical properties on temperature. At 300K, the structure exhibited the highest tensile strength, with a peak stress found to be around 4.5 GPa. This high strength is indicative of robust interatomic bonds at a relatively low temperature. At 1000K, the peak tensile stress decreased notably to approximately 3.7 GPa, suggesting that increased temperature began to weaken the load-carrying capacity. At 2000K, a further reduction in peak stress to about 2.8 GPa was observed. At 3000K, the material showed a significant decrease in tensile strength, with the peak stress dropping below 2.0 GPa. The tensile strength and the ability of the material to withstand deformation without yielding decreases with increasing temperature as evident in Fig. 5c. This trend is expected due to the thermal agitation of atoms, which interferes with the stability of the crystal lattice and weakens the

overall strength of the g-TPMS. The behavior of the W g-TPMS lattice structure is in line with conventional materials, which generally exhibit decreased tensile strength and increased ductility at higher temperatures.

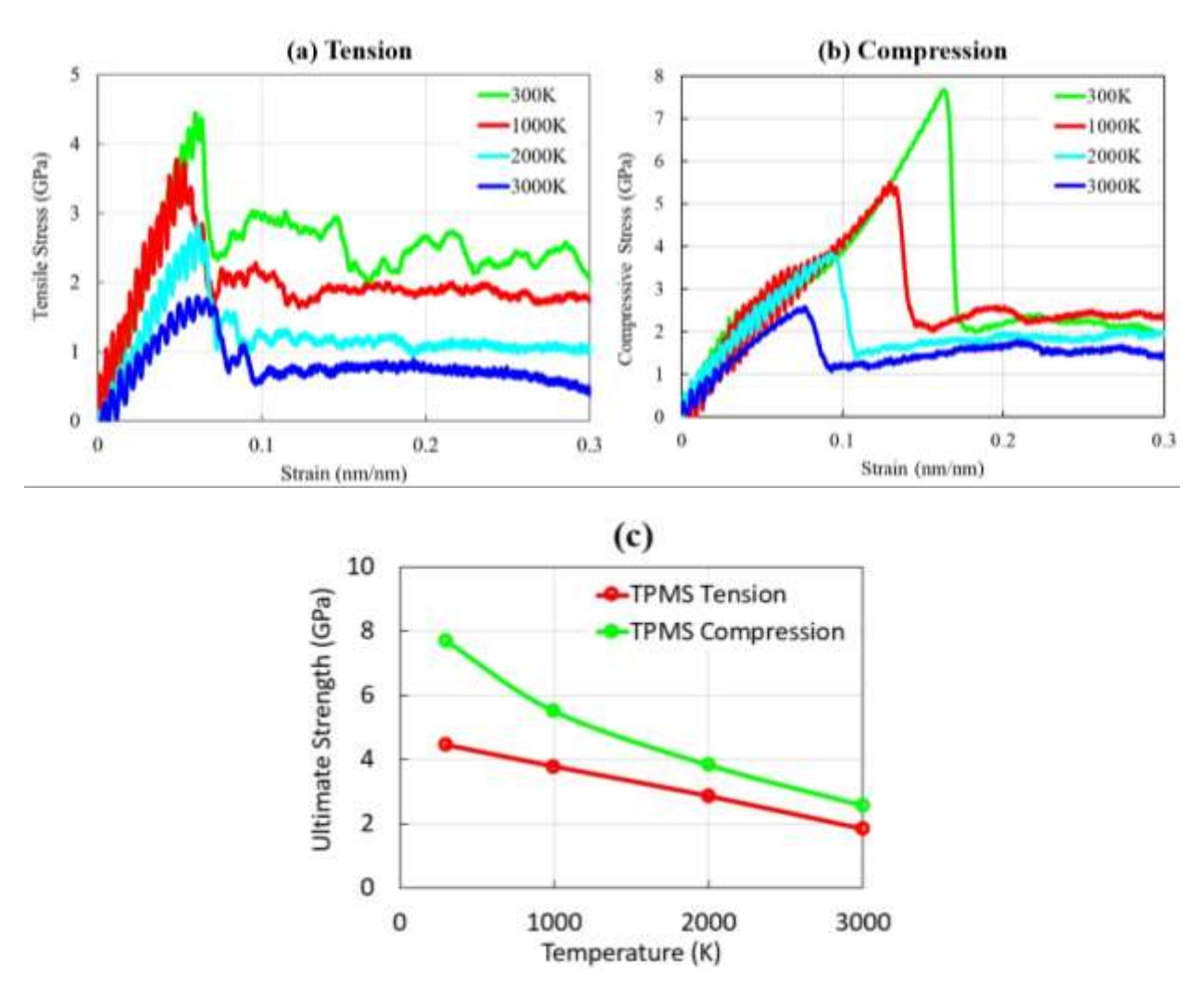


Figure. 5. Themo-mechanical response of W g-TPMS structure: (a) Tensile loading, (b) compressive loading, (c) Effect of temperature ultimate strength.

The Figure as shown in Fig. 5b represents the compressive response of a W g-TPMS lattice structure subjected to varying temperatures. The compressive response of the g-TPMS lattice structure was examined at temperatures of 300K, 1000K, 2000K, and 3000K. As the temperature increases, there is a noticeable degradation both in tensile and compressive strength as indicated in Fig. 5a. . The data suggests a clear trend of decreasing tensile and compressive strength and strain with increasing temperature in the g-TPMS lattice structure. At room temperature i.e., 300K, the structure demonstrates the highest tensile strength. However, as the temperature rises to 1000K

and beyond, thermal softening likely occurs, as evidenced by the reduction in ultimate tensile and compressive strength. The most dramatic changes are observed at 3000K, where the compressive strength is significantly reduced. The graphical representation in Fig. 5c indicates a decrease in compressive strength (ultimate compressive strength) by 66.5%, whereas for tensile loading this decrement is 58.4%. It is possible that at such high temperatures, atomic vibration or mobility in the material increased and the bonds within the material are significantly weakened, leading to reduced resistance to the applied load, which could dramatically affect its mechanical properties.

3.5 He Interstitials Effect on Tensile Response

Applications those requiring high strength and reliability, such as in nuclear reactors, the presence of helium interstitials poses a significant challenge. The increased variability in the stress-strain response at higher helium concentrations suggests that predicting the failure point becomes more difficult, which could be a critical concern for structural stability and safety. Thus, to investigate the effect of Helium (He) interstitials in W, the present study considers both W g-TPMS and bulk W. For g-TPMS present study considers only 38.9% volume fraction lattice structure as a representative model. The tensile tests were conducted on both g-TPMS and bulk W with varying concentrations of helium interstitials (1%, 5%, 10%, and 15%). The study reveals significant changes in the mechanical response of both W g-TPMS and bulk W samples with He interstitials compared to the pristine or He-free samples.

The pristine bulk W sample exhibited the highest tensile strength, reaching a peak stress of nearly 26.3 GPa (Fig. 6b), indicating the robust nature of defect-free W under tensile loading. The introduction of 1% helium interstitials resulted in a decrease in ultimate tensile stress to about 23.6 GPa i.e., 10% reduction in strength, suggesting a moderate level of disruption to the lattice integrity of g-TPMS. As the helium concentration increased to 5%, further reduction in peak tensile stress was observed i.e., 40.7%, along with an increase in the fluctuation of stress values post-yielding, indicative of the compromised structural consistency of the material. With 10% helium interstitials, the peak stress continued to decline by 56.7%, and the stress-strain curve showed even greater fluctuations, reflecting the significant impact of helium on the mechanical stability of the g-TPMS. At 15% helium interstitials, the UTS was drastically reduced, with the peak value dropping around 10.6 GPa i.e., 60%, and a highly irregular post-peak response was observed, indicating severe lattice degradation due to the higher concentration of helium interstitials.

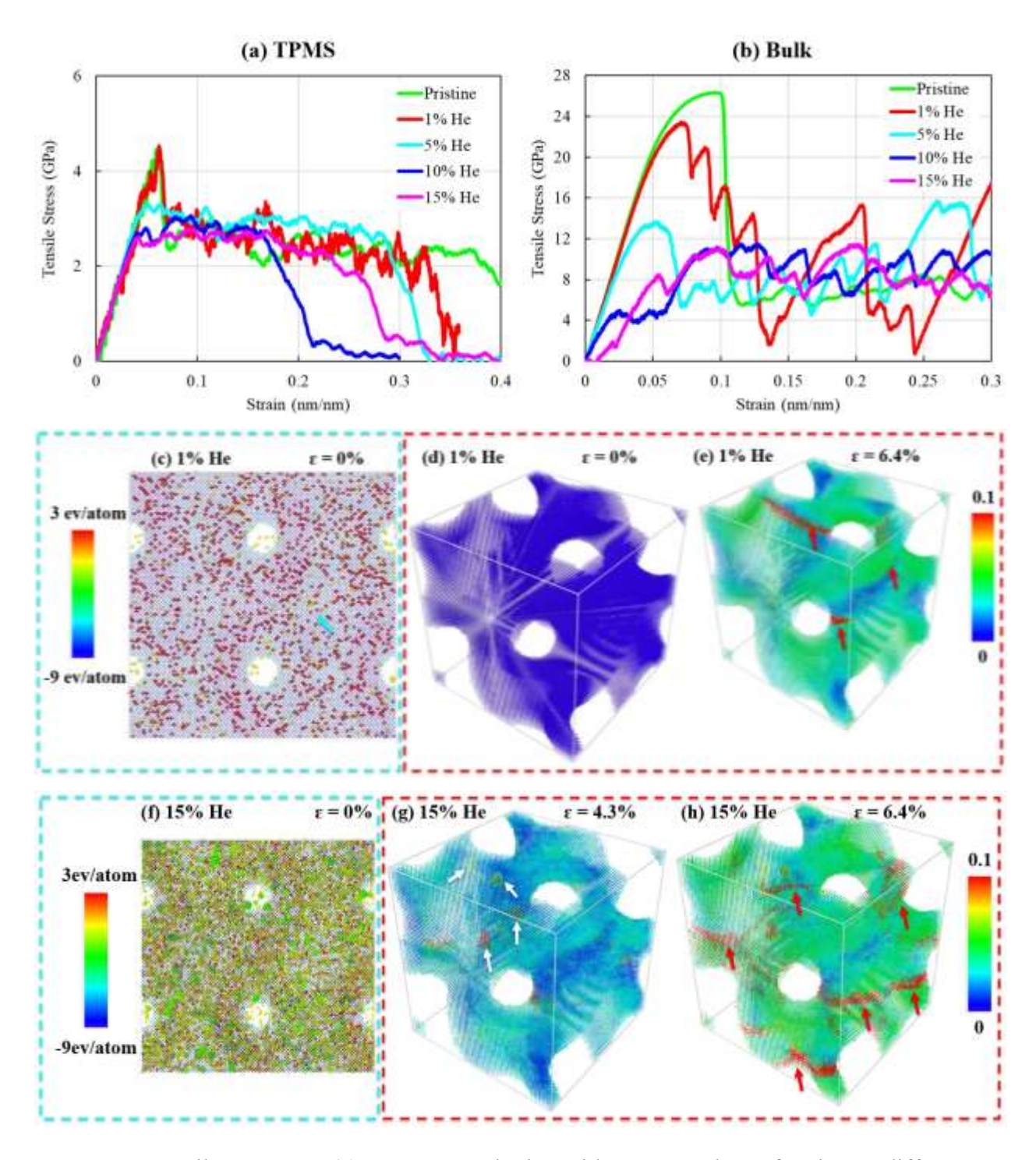


Figure. 6. Tensile response: (a) W g-TPMS lattice with 38.9% volume fraction at different He interstitials concentration, (b) Bulk W at different He interstitials concentration, (c) potential energy distribution after 1% He interstitials introduction (red color atoms indicates He), Shear strain distribution: (d) strain = 0, (e) strain = 6.4%, (f) potential energy distribution after 15% He

interstitials introduction (He cluster/bubble formation indicated by green color), Shear strain distribution: (g) strain = 4.3%, and (h) strain = 6.4%.

The observed decline in UTS with increasing helium concentration is likely due to the disruption of the W lattice by helium atoms interstitials. Localized stress concentrations around these interstitials facilitate premature yielding and failure (Fig. 6g). The potential energy distribution also depicts that these He atoms (red color in Fig. 6c and green color in Fig. 6f) are at higher energy state. The behavior of tungsten with He interstitials is consistent with known phenomena of radiation damage and helium embrittlement in metals, where interstitial atoms lead to material weakening. The high tensile strength of pristine W confirms its suitability for high-stress applications, such as in fusion reactors where tungsten is used as a plasma-facing material due to its high melting point and strength. However, the susceptibility of tungsten to helium-induced damage must be considered in environments where helium accumulation is likely, as even low concentrations of helium significantly compromise the mechanical properties of the W.

In addition to bulk W, tensile tests were also conducted on the W g-TPMS lattice structures to understand the influence of helium interstitials at different concentrations (1%, 5%, 10%, and 15%) as shown in Fig. 6a. The pristine sample (t = 2 nm or volume fraction 38.9%), with no helium interstitials, exhibited the highest tensile strength, reaching UTS of nearly 4.5 GPa. This represents the intrinsic strength of the material without any defects or impurities. However, unlike the bulk W sample, introducing 1% helium interstitials does not change the mechanical properties significantly of the W g-TPMS structure. Introducing 5% helium interstitials resulted in a noticeable reduction in ultimate stress, down to approximately 3.3 GPa i.e., 26%, suggesting that a moderate amount of helium can significantly impact the tensile properties of the g-TPMS. At 10% helium interstitials, the UTS further decreased, indicating that helium may cause localized weakening or variation in the g-TPMS. The 10% and 15% helium interstitial samples showed a substantial reduction in peak stress around or below 3.0 GPa, and the material exhibited a high degree of variability in its response to the tensile loading, demonstrating a pronounced weakening effect due to the presence of helium. The reduction in UTS with increasing helium concentration suggests that helium interstitials are defects within the tungsten lattice, disrupting its structural integrity and decreasing its ability to resist external tensile loads. The potential energy distribution is high around these He interstitials as shown in Fig. 6c and 6f. These He atoms or bubbles are also associated with localized high-shear strain fields. Thus, these Helium interstitials likely create

regions of stress concentration, which could facilitate the initiation and propagation of voids or cracks under tensile loading. To summarize, the presence of helium interstitials exacerbates material response. The findings are consistent with studies on other metals and alloys where interstitial impurities, such as hydrogen, are known to cause embrittlement [74-76].

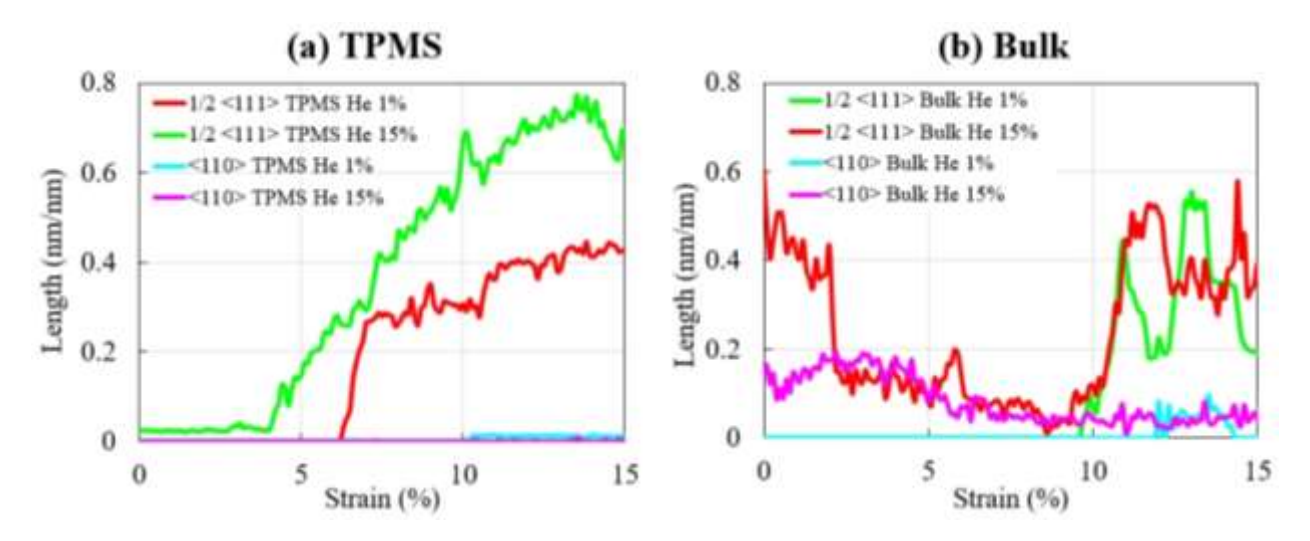


Figure. 7. Dislocation evolution during tensile loading: (a) W g-TPMS lattice structure, (b) Bulk W.

To delineate the deformation mechanism present study also investigates dislocation analysis on these structures as shown in in Fig. 7. The helium interstitials affect the dislocation behavior in bulk W, and the effect is quite different in g-TPMS W lattice structure compared to the bulk W. At 1% He both g-TPMS and Bulk TPMs do not introduce any dislocation prior to the application of external load. Dislocations evolve only at the onset of plastic deformation for 1% He interstitials. Plastic deformation is dominated by ½ <111> dislocation for both cases. However, at 15% He both structures contain dislocations even before the application of the external load. In addition to ½ <111>, bulk W generates a significant amount of <110> dislocation at 15% He interstitials. At 15% He interstitials both structures show a more significant increase in dislocation length compared to 1% He interstitials, which could indicate a greater sensitivity to helium embrittlement. The variability introduced by helium impurities into the tensile response of the material highlights the importance of considering such effects in the design of W-based fusion reactors.

4.0 Conclusion

The study advances the understanding of material behavior at the nanoscale and opens new possibilities for the application of W g-TPMS lattice structure for advanced technological applications such as nuclear fusion reactors. The outcomes of the present study can be summarized as follows:

- Mechanical properties are nearly identical in three principles loading direction of W g-TPMS structures, evident from consistent stress-strain responses in all three directions (X, Y and Z) under both tensile and compressive loading.
- 2. Tensile testing of g-TPMS lattices reveals that structures with higher volume fractions exhibit greater tensile strength but reduced ductility. Conversely, lattice structures with lower volume fractions are more ductile but less strong. This inverse relationship between strength and ductility suggests that mechanical properties can be finely tuned through the design of volume fractions in these lattice structures.
- 3. The study investigates the impact of temperature on the mechanical properties of W g-TPMS lattices at 300K, 1000K, and 2000K. The tensile strength decreases progressively with increasing temperature. This trend, attributed to thermal agitation affecting the crystal lattice, aligns with conventional engineering material behavior under temperature variation but may be influenced by the unique architecture of the g-TPMS.
- 4. The Poisson's ratio of g-TPMS structures is found to be dependent on volume fraction. As the volume fraction increases, the Poisson's ratio approaches a plateau value that is close to that of bulk tungsten.
- 5. The tensile and compressive response of both W g-TPMS and bulk W are significantly affected by the presence of helium interstitials, with a clear trend of decreasing tensile strength and mechanical stability as helium concentration rises.

The present study enhances the understanding of the mechanical properties of g-TPMS W lattice structures. Moreover, the study indicates helium embrittlement in W g-TPMS and offers a foundation for developing strategies to counteract these effects in critical applications where material integrity is paramount. The results contribute to the growing body of research on helium effects in materials used in environments where helium accumulation is expected, such as in fusion reactors. While this study provides significant insights into the mechanical properties of W g-TPMS structures, it is important to recognize certain limitations. The atomistic simulations used here, while detailed, are inherently limited by the scale and complexity of the models that can be

practically simulated. Future work should aim to extend these findings through experimental validation, particularly at larger scales and under more varied environmental conditions, with different geometries and materials. Additionally, the study primarily focuses on tensile and compressive loading scenarios. Future research could explore the mechanical behavior of W g-TPMS structures under different loading conditions such as shear, torsion, and cyclic loading, which are also relevant for real-world applications.

5.0 Acknowledgement

ZI is thankful to the National Science Foundation (NSF) Award Number: 2206952. ZI is also thankful to Bowling Green State University, School of Engineering Faculty Start-Up Grant 33900032: SU Islam.

6.0 Conflict of Interest:

On behalf of all authors, the corresponding author states that there is no conflict of interest.

References

- 1. Shen, L., et al., *Tungsten extractive metallurgy: A review of processes and their challenges for sustainability.* Minerals Engineering, 2019. **142**: p. 105934.
- 2. Trasorras, J.R., et al., *Tungsten, tungsten alloys, and tungsten compounds*. Ullmann's Encyclopedia of Industrial Chemistry, 2000: p. 1-53.
- 3. Trasorras, J.R.L., et al., *Tungsten, Tungsten Alloys, and Tungsten Compounds*, in *Ullmann's Encyclopedia of Industrial Chemistry*. 2016. p. 1-53.
- 4. Penrice, T.W., *Tungsten and Tungsten Alloys*, in *Kirk-Othmer Encyclopedia of Chemical Technology*. 2010. p. 1-15.
- 5. Hou, Q.-Q., et al., *Microstructure and its high temperature oxidation behavior of W-Cr alloys prepared by spark plasma sintering*. Materialia, 2019. **6**: p. 100332.
- 6. Das, S., et al., *Hardening and Strain Localisation in Helium-Ion-Implanted Tungsten*. Scientific Reports, 2019. **9**(1): p. 18354.
- 7. Sprouster, D.J., et al., *Irradiation-Dependent Helium Gas Bubble Superlattice in Tungsten*. Scientific Reports, 2019. **9**(1): p. 2277.

- 8. Huang, X., C. Lv, and H. Chu, *Anomalous shape effect of nanosized helium bubble on the elastic field in irradiated tungsten.* Scientific Reports, 2021. **11**(1): p. 830.
- 9. Dürrschnabel, M., et al., *New insights into microstructure of neutron-irradiated tungsten.* Scientific Reports, 2021. **11**(1): p. 7572.
- 10. Lang, E., et al., Examination of Early-Stage Helium Retention and Release in Dispersion-Strengthened Tungsten Alloys. Fusion Science and Technology, 2023. **79**(5): p. 592-601.
- 11. Buzi, L., et al., *Deuterium and helium ion irradiation of nanograined tungsten and tungsten–titanium alloys.* Nuclear Materials and Energy, 2019. **21**: p. 100713.
- 12. El-Atwani, O., et al., *In-situ irradiation tolerance investigation of high strength ultrafine tungsten-titanium carbide alloy*. Acta Materialia, 2019. **164**: p. 547-559.
- 13. Iwakiri, H., et al., *Microstructure evolution in tungsten during low-energy helium ion irradiation*. Journal of Nuclear Materials, 2000. **283-287**: p. 1134-1138.
- 14. Tokunaga, K., et al., *Synergistic effects of high heat loading and helium irradiation of tungsten.* Journal of Nuclear Materials, 2004. **329-333**: p. 757-760.
- 15. Xu, Q., N. Yoshida, and T. Yoshiie, *Accumulation of helium in tungsten irradiated by helium and neutrons*. Journal of Nuclear Materials, 2007. **367-370**: p. 806-811.
- 16. Harrison, R.W., et al., A study of the effect of helium concentration and displacement damage on the microstructure of helium ion irradiated tungsten. Journal of Nuclear Materials, 2017. **495**: p. 492-503.
- 17. Ueda, Y., et al., Simultaneous irradiation effects of hydrogen and helium ions on tungsten. Journal of Nuclear Materials, 2009. **386-388**: p. 725-728.
- 18. Wadsworth, J., T. Nieh, and J. Stephens, *Recent advances in aerospace refractory metal alloys*. International materials reviews, 1988. **33**(1): p. 131-150.
- 19. Pan, S.-H., et al., *Additive manufacturing of tungsten, tungsten-based alloys, and tungsten matrix composites.* Tungsten, 2023. **5**(1): p. 1-31.
- 20. Satya Prasad, V., R. Baligidad, and A.A. Gokhale, *Niobium and other high temperature refractory metals for aerospace applications*. Aerospace Materials and Material Technologies: Volume 1: Aerospace Materials, 2017: p. 267-288.
- 21. Helou, M. and S. Kara, *Design, analysis and manufacturing of lattice structures: an overview.* International Journal of Computer Integrated Manufacturing, 2018. **31**(3): p. 243-261.

- 22. Maconachie, T., et al., *SLM lattice structures: Properties, performance, applications and challenges.* Materials & Design, 2019. **183**: p. 108137.
- 23. Köhnen, P., et al., Mechanical properties and deformation behavior of additively manufactured lattice structures of stainless steel. Materials & Design, 2018. **145**: p. 205-217.
- 24. Catchpole-Smith, S., et al., *Thermal conductivity of TPMS lattice structures*manufactured via laser powder bed fusion. Additive Manufacturing, 2019. **30**: p. 100846.
- 25. Yu, S., J. Sun, and J. Bai, *Investigation of functionally graded TPMS structures* fabricated by additive manufacturing. Materials & Design, 2019. **182**: p. 108021.
- 26. Al-Ketan, O., et al., Functionally graded and multi-morphology sheet TPMS lattices:

 Design, manufacturing, and mechanical properties. Journal of the Mechanical Behavior of Biomedical Materials, 2020. 102: p. 103520.
- 27. Teng, F., et al. *Topological and Mechanical Properties of Different Lattice Structures Based on Additive Manufacturing*. Micromachines, 2022. **13**, DOI: 10.3390/mi13071017.
- 28. Dar, U.A., et al., Experimental and numerical investigation of compressive behavior of lattice structures manufactured through projection micro stereolithography. Materials Today Communications, 2020. **25**: p. 101563.
- 29. Nasim, M. and U. Galvanetto, *Mechanical characterisation of additively manufactured*PA12 lattice structures under quasi-static compression. Materials Today

 Communications, 2021. **29**: p. 102902.
- 30. Xue, X., et al., *Lattice structures with negative Poisson's ratio: A review.* Materials Today Communications, 2023. **34**: p. 105132.
- 31. Sahariah, B.J., A. Namdeo, and P. Khanikar, *Composite-inspired multilattice metamaterial structure: An auxetic lattice design with improved strength and energy absorption.* Materials Today Communications, 2022. **30**: p. 103159.
- 32. Deng, Y., et al., Experimental and numerical studies on the compression responses of novel mixed lattice structures. Materials Today Communications, 2022. **33**: p. 104439.
- 33. Mueller, J. and K. Shea, *Buckling, build orientation, and scaling effects in 3D printed lattices*. Materials Today Communications, 2018. **17**: p. 69-75.

- 34. Dara, A., et al., Numerical and experimental investigations of novel nature inspired open lattice cellular structures for enhanced stiffness and specific energy absorption. Materials Today Communications, 2022. **31**: p. 103286.
- 35. Xia, B., et al., *The arrangement patterns optimization of 3D honeycomb and 3D re*entrant honeycomb structures for energy absorption. Materials Today Communications, 2023. **35**: p. 105996.
- 36. Qin, Z., et al., The mechanics and design of a lightweight three-dimensional graphene assembly. Science Advances. **3**(1): p. e1601536.
- 37. Abueidda, D.W., et al., *Mechanical properties of 3D printed polymeric Gyroid cellular structures: Experimental and finite element study.* Materials & Design, 2019. **165**: p. 107597.
- 38. Dolan, J.A., et al., *Optical Properties of Gyroid Structured Materials: From Photonic Crystals to Metamaterials.* Advanced Optical Materials, 2015. **3**(1): p. 12-32.
- 39. Oh, S.S., et al., *On the Origin of Chirality in Nanoplasmonic Gyroid Metamaterials*. Advanced Materials, 2013. **25**(4): p. 612-617.
- 40. Fu, T., et al., *Oxidation protection of tungsten alloys for nuclear fusion applications: A comprehensive review.* Journal of Alloys and Compounds, 2021. **884**: p. 161057.
- 41. Fukuda, M., A. Hasegawa, and S. Nogami, *Thermal properties of pure tungsten and its alloys for fusion applications*. Fusion Engineering and Design, 2018. **132**: p. 1-6.
- 42. Nogami, S., et al., *Tungsten–tantalum alloys for fusion reactor applications*. Journal of Nuclear Materials, 2022. **566**: p. 153740.
- 43. Fu, T., et al., *Oxidation protection of tungsten alloys for nuclear fusion applications: A comprehensive review.* Journal of Alloys and Compounds, 2021. **884**: p. 161057.
- 44. Wu, Y., Manufacturing of tungsten and tungsten composites for fusion application via different routes. Tungsten, 2019. **1**(1): p. 80-90.
- 45. Saha, S.K., et al., *Scalable submicrometer additive manufacturing*. Science, 2019. **366**(6461): p. 105-109.
- 46. WU, Y., Research progress in irradiation damage behavior of tungsten and its alloys for nuclear fusion reactor. Acta Metall Sin, 2019. **55**(8): p. 939-950.
- 47. Rieth, M., et al., *Behavior of tungsten under irradiation and plasma interaction*. Journal of Nuclear Materials, 2019. **519**: p. 334-368.

- 48. Qanbarian, M., et al., *Molecular dynamics investigation of argon evaporation on copper surfaces covered with graphene and carbon nanotubes*. Materials Today Communications, 2024. **38**: p. 107900.
- 49. Sarkar, P.K., N. Mitra, and J.S. Dolado, *Thermal conductivity of layered minerals using molecular dynamics simulation: A case study on calcium sulfates.* Materials Today Communications, 2024. **38**: p. 108101.
- 50. He, T., et al., Molecular dynamics for nanoindentation in the γ/α2 interfacial strengthening mechanism of a duplex full lamellar TiAl alloy. Materials Today Communications, 2024. **38**: p. 107965.
- 51. Li, G., et al., Effect of Al related chemical short-range order on the irradiation resistance of Al0.5CoCrFeNi multi-principal element alloy: A molecular dynamics simulation.

 Materials Today Communications, 2024. 38: p. 108302.
- 52. Zhang, Y., et al., *Molecular dynamics simulation of C-S-H corrosion in chloride environment.* Materials Today Communications, 2022. **33**: p. 104568.
- 53. Mahboob, M. and M. Zahabul Islam, *Molecular dynamics simulations of defective CNT-polyethylene composite systems*. Computational Materials Science, 2013. **79**: p. 223-229.
- Najafi, G., M. Mosavi Mashhadi, and M.M. Seyyed Fakhrabadi, *Reinforcement of polymer nanocomposites by a-graphyne nanotubes: A multiscale simulation*.
 Computational Materials Science, 2021. 194: p. 110431.
- 55. Peng, H.R., et al., Uncovering the softening mechanism and exploring the strengthening strategies in extremely fine nanograined metals: A molecular dynamics study. Journal of Materials Science & Technology, 2022. 109: p. 186-196.
- 56. Hua, D., et al., *Molecular dynamics simulation of the tribological performance of amorphous/amorphous nano-laminates*. Journal of Materials Science & Technology, 2022. **105**: p. 226-236.
- 57. Zhou, J., et al., *Molecular dynamics simulation of reinforcement mechanism of graphene/aluminum composites and microstructure evolution.* Journal of Materials Research and Technology, 2023. **23**: p. 2147-2159.
- 58. Xie, Y., et al., A computational study of the effect of external heat flux and electric field on the nano-pumping of C20 molecules in carbon nanotubes by molecular dynamics simulation. Journal of Materials Research and Technology, 2023. 25: p. 1898-1908.

- 59. Hu, X., et al., *Irradiation hardening of pure tungsten exposed to neutron irradiation.*Journal of Nuclear Materials, 2016. **480**: p. 235-243.
- 60. Jiang, J., P. Chen, and W. Sun, *Monitoring micro-structural evolution during aluminum sintering and understanding the sintering mechanism of aluminum nanoparticles: A molecular dynamics study.* Journal of Materials Science & Technology, 2020. **57**: p. 92-100.
- 61. Mahata, A., T. Mukhopadhyay, and M. Asle Zaeem, *Liquid ordering induced heterogeneities in homogeneous nucleation during solidification of pure metals.* Journal of Materials Science & Technology, 2022. **106**: p. 77-89.
- 62. Li, J., et al., *Microstructure evolution and deformation mechanism of amorphous/crystalline high-entropy-alloy composites*. Journal of Materials Science & Technology, 2020. **54**: p. 14-19.
- 63. Bonny, G., P. Grigorev, and D. Terentyev, *On the binding of nanometric hydrogen–helium clusters in tungsten*. Journal of Physics: Condensed Matter, 2014. **26**(48): p. 485001.
- 64. Thompson, A.P., et al., *LAMMPS a flexible simulation tool for particle-based materials modeling at the atomic, meso, and continuum scales.* Computer Physics Communications, 2022. **271**: p. 108171.
- 65. nTop, *nTop Inc.*, *https://www.ntop.com/*.
- 66. Rodrigo, C., et al., *Quasi-static and dynamic compression of additively manufactured functionally graded lattices: Experiments and simulations.* Engineering Structures, 2023. **284**: p. 115909.
- 67. Michael Bauccio, E., *ASM Metals Reference Book*. Third ed. 1993, Materials Park, OH: ASM International.
- 68. Ross, R.B., Metallic Materials Specification Handbook. 1992, Chapman & Hall, London.
- 69. Shi, S., et al., Scaling behavior of stiffness and strength of hierarchical network nanomaterials. Science, 2021. **371**(6533): p. 1026-1033.
- 70. Arzt, E., Size effects in materials due to microstructural and dimensional constraints: a comparative review. Acta Materialia, 1998. **46**(16): p. 5611-5626.

- 71. He, C.-Y., et al., Size-dependent deformation mechanisms in copper gradient nanograined structure: A molecular dynamics simulation. Materials Today Communications, 2022. **31**: p. 103198.
- 72. Gibson, I. and M.F. Ashby, *The mechanics of three-dimensional cellular materials*. Proceedings of the royal society of London. A. Mathematical and physical sciences, 1982. **382**(1782): p. 43-59.
- 73. Ashby, M.F., et al., *Metal foams: a design guide*. 2000: Elsevier.
- 74. Li, X., et al., *Hydrogen embrittlement and failure mechanisms of multi-principal element alloys: A review.* Journal of Materials Science & Technology, 2022. **122**: p. 20-32.
- 75. Xu, J., et al., *Hydrogen embrittlement behavior of selective laser-melted Inconel 718 alloy.* Journal of Materials Research and Technology, 2023. **23**: p. 359-369.
- 76. Norouzi, E., et al., *Hydrogen embrittlement behavior in FeCCrNiBSi TRIP steel.* Journal of Materials Research and Technology, 2023. **23**: p. 859-868.